Article

Temperature Self-Adaptive Ultra-Thin Solar Absorber Based on Optimization Algorithm

Jian Chen [1,†], Xin Li [1,†], Yutai Chen [1], Zhaojian Zhang [1], Yang Yu [1], Xin He [1], Huan Chen [1], Junbo Yang [1,*], Zhenfu Zhang [1] and Xiaopeng Yao [2]

1 College of Sciences, National University of Defense Technology, Changsha 410073, China
2 School of Medical Information and Engineering, Southwest Medical University, Luzhou 646000, China
* Correspondence: yangjunbo@nudt.edu.cn
† These authors contributed equally to this work.

Abstract: In solar applications, the solar absorber is paramount to converting solar radiation to heat energy. We systematically examined the relationship between the efficiency of the solar absorber and operating temperature and other factors. By combining inverse designs with surface plasmonic and Fabry-Perot cavity solar absorption theories, we have developed several solar absorber devices with excellent performance at different temperatures. One of these devices displays a solar spectral absorption of 95.6%, an ultra-low emission rate of 5.7%, and optical-to-thermal conversion efficiency exceeding 90%, all within an ultra-thin depth of 0.45 μm under working temperatures of 600 K. The device has the potential to surpass the Shockley-Queisser limit (S-Q limit) in solar power generation systems. Our method is adaptable, enabling the design of optimal-performance devices to the greatest extent possible. The design was optimized using modern optimization algorithms to meet complex conditions and offers new insights for further study of the conversion from solar to thermal energy and the advancement of solar energy applications.

Keywords: the solar absorber; optical metasurface; optimization algorithm

1. Introduction

Utilizing solar energy provides a potent solution to the challenges posed by energy depletion and environmental degradation due to the abundance and renewability of solar resources. To harness this potential, solar absorbers [1,2] can convert light into heat energy, which can then be utilized in various fields such as high-temperature heterogeneous catalysis, anti-bacterial treatments, and photothermal power generation [3], as depicted in Figure 1. The efficacy of this transformation process depends significantly on the solar absorber's ability to convert solar energy into heat energy. The incorporation of thermoelectric conversion devices, such as thermophotovoltaics and heat engines, in solar energy systems holds the potential to surpass the Shockley-Queisser limit [4], which sets the theoretical maximum efficiency of a single p-n junction solar energy cell at 33.7% [5,6]. This efficiency limit results from the loss of photon energy in the high-frequency band. Furthermore, photothermal power generation technology exhibits excellent energy storage and regulation capability through heat storage media [7,8], making it a valuable addition to the development of the solar system and enhancing the growth of green renewable energy.
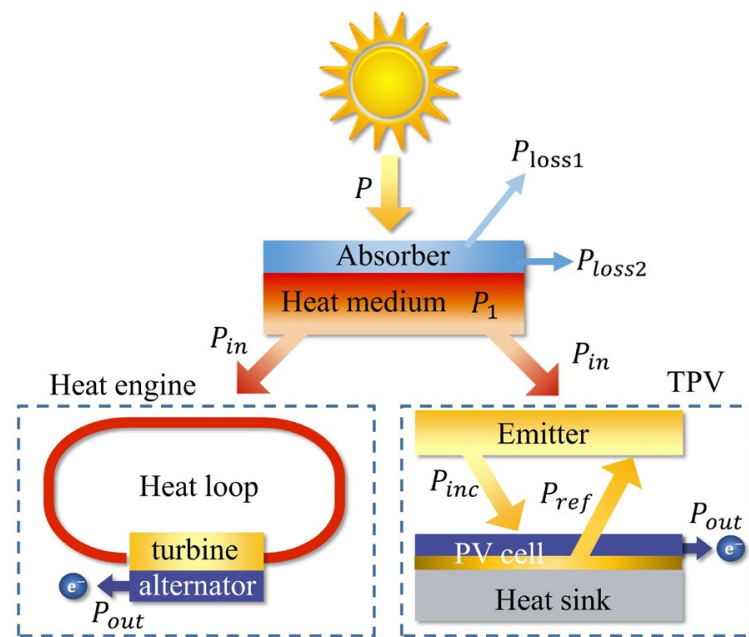
Figure 1. Application of the solar absorber: For the solar energy of power P, reflection loss, represented by P_{loss1}; thermal radiation and conduction loss, represented by P_{loss2}. The absorbed solar energy power, P_1, is stored in a heat medium and then used by heat energy utilization systems such as TPV and heat engines.

A great deal of research has been conducted to explore solar absorbers in recent decades. Researchers have made strides in achieving high-efficiency solar absorption by utilizing metal-insulator-metal (MIM) resonator structures [9]. To further improve device performance, refractory metals with good plasmon resonance properties, such as Ti, W, Cr, and V, have been used. For instance, Li et al. designed an ultra-wideband perfect absorber using a titanium metal-insulator composite multilayer (MICM) layer [10], achieving an average absorption rate of 97% in the wavelength range of 570 nm to 3539 nm. The performance of solar absorbers, such as their emissivity and absorptivity, also plays a vital role in their effectiveness. As such, it is essential to adjust these factors to enhance their performance. To achieve this, Farber proposed the development of selective solar absorbers that maximize absorption in the solar concentration band while minimizing absorption in other regions [1]. This approach reduces radiation power loss, thereby improving the light-to-heat conversion efficiency of the solar absorber. Traditional design methods use fundamental principles to guide the design of specific structured devices, and theoretical or empirical methods are employed to optimize optical characteristics such as filtering [11], absorption [12], and polarization conversion [13]. However, the optimization ability of this approach diminishes with device structure and spectral response complexities, such as patterned optical structures [14] and selective absorption [15]. A reverse design has emerged as a promising method for the design of solar absorbers with tailored absorption curves. In a reverse design [14], optimization algorithms, such as genetic algorithms, particle swarm optimization, and simulated annealing, are used to modify the device's structure, shape, material, and size to rapidly identify optimal devices. For instance, an absorber designed by Liu et al. achieved an average absorption efficiency of 98% over a range of 300 nm to 2500 nm [16]. Zhang et al. utilized the Multi-Island Genetic Algorithm (MIGA) to design an absorber that achieved solar absorptivity greater than 0.932 and mid-infrared emissivity lower than 0.058 [17].

The implementation scenarios of solar absorbers have a significant impact on device performance. Therefore, Klaus Burlafinger et al. thoroughly investigated the effects of cutoff wavelength, concentration ratio, and operating temperature on performance [18]. Furthermore, based on the exploration of the effects of cutoff wavelength, concentration

ratio, and operating temperature, Feng Cao et al. designed a solar absorber made of iron-chromium alloys, exhibiting high solar spectral absorptivity and low infrared radiation transmissivity [19]. Davide et al. further designed absorbers optimized for specific working scenarios and conducted a detailed discussion on the adaptability of device operating temperature [20].

In this paper, we adopted a reverse design method to design a structure super-surface to maximize the light-to-heat conversion efficiency of the absorber. We designed a super-surface structure array, as shown in Figure 2, and selected four high-temperature resistant metal materials (Ti, Cr, W, and V) as the absorbing materials, stacking 2–4 layers of SiO_2 and metal discs alternately on the metal substrate. Then, through the reverse design method, we optimized the height and diameter of each disc to obtain the device applicable to different scenarios. We analyzed the achievable efficiency in the solar-thermal system, possibly surpassing the S-Q limit, and discussed the insensitivity of the device to angles and polarization. The proposed super-surface device design method based on the optimization algorithm not only maximizes the light-to-heat conversion efficiency but also provides new ideas for designing absorbers under different operating conditions. In addition, this design method also has potential applications such as selective emitters [21] and infrared stealth [22].
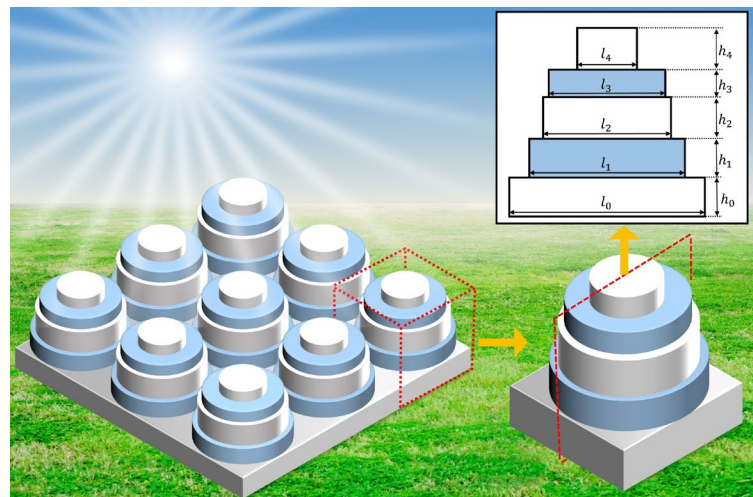

Figure 2. Schematic diagram of disk array absorber. Metasurface absorber stacks multiple layers of metal and SiO_2. Illustrations represent cross sections along diameters. $(l_1 - l_4)$ represents the diameters of the disks stacked in the structure the from largest to smallest, while $(h_1 - h_4)$ represents the thicknesses of the disks corresponding to diameters $(h_1 - h_4)$.

2. Methods

2.1. Structure and Design Methods

In Figure 2, the three-dimensional structure and central cross-section diagrams of the disc absorber are presented. The device is composed of alternating layers of SiO_2 and metal materials. With a highly reflective metal of sufficient thickness, the substrate exhibits a transmittance of 0. The absorption efficiency increases with the number of stacking layers. However, the production cost and marginal effect also increase. Hence, the maximum number of stacking layers is set to 4, which has demonstrated superior performance. The thickness of the metal substrate is denoted as h_0, and the period of the array is denoted as l_0. The diameter of the discs, starting from the largest to smallest, are $(l_1 - l_4)$, with corresponding thicknesses of $(h_1 - h_4)$, respectively.

The design flow for the above structural parameters is shown in Figure 3:

1. Generation of m metal substrate devices.
2. For each device, the i-th disk of random size was stacked, and the metal material and SiO_2 of the disk were stacked alternately, and the parameters of the disk were (l_i, h_i).

3. The spectral characteristics of the device with structure parameter ($l_0 \sim l_i, h_1 \sim h_i$) were calculated by Maxwell equation.
4. To determine whether a device satisfies the requirement of target function. If it is satisfied, go to Step 6. If it does not satisfy, go to Step 2.
5. The structure parameter ($l_0 \sim l_i, h_1 \sim h_i$) of the device is iterated k times by the iterative method of PSO, and a new set of devices is obtained and transferred to Step 4.
6. Output of the structural parameters and spectral characteristics of the final devices that meet the target function criteria.
7. To determine whether the current output device has the 4-layer stack disk, if satisfied, return to Step 2, otherwise, end the process.
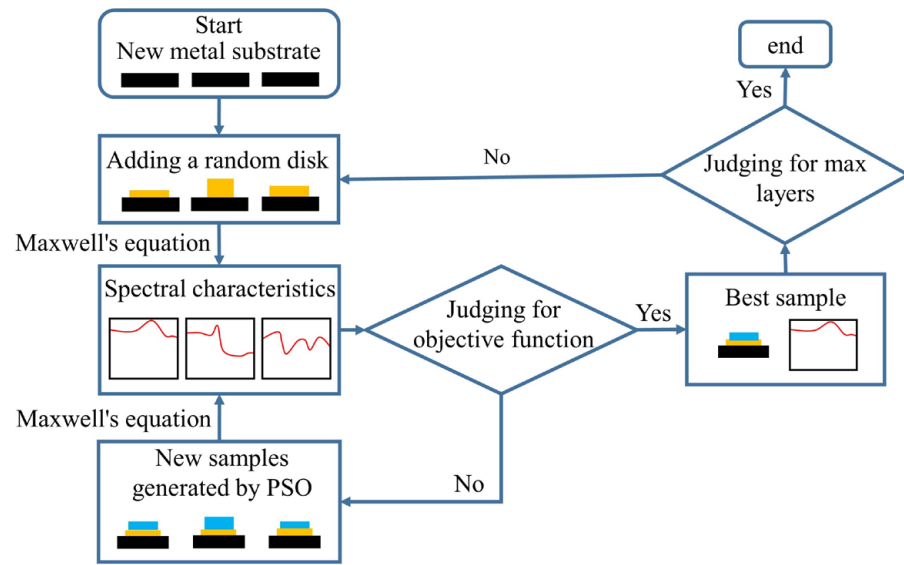
Figure 3. Design flow of the solar energy absorber.

In Step 3, the Finite Difference Time Domain Method (FDTD) is employed to approximately solve Maxwell's equations. The commercial software Lumerical FDTD Solutions was utilized for calculations. The Particle Swarm Optimization (PSO) method in Step 5 seeks the optimal solution through collaboration and information sharing among individuals in a group. It combines individual and global optimums, increasing the likelihood of reaching the global optimum. Specifically, the structural parameters of each of the generated m devices are represented as positions $X_k = (l_0 \sim l_i, h_1 \sim h_4)$ with a defined velocity $V_k = (v_1, v_2, \ldots, v_N)$. The fitness value of each device $F(X_k)$ is calculated from the spectral features in Step 3. Each device also has a historical optimal fitness value $F(p_{best})$ and its corresponding p_{best}. It has a historical value $F(g_{best})$ and its corresponding g_{best} among all devices. The iterative formula for one of the devices is as follows:

$$V_{k+1} = V_k + C_1 rand(0,1)(p_{best} - X_k) + C_2 rand(0,1)(g_{best} - X_k) \tag{1}$$

$$X_{k+1} = X_k + w * V_{k+1} \tag{2}$$

The coefficients in the equation are determined as $C_1 = -3.7 \times k/itr + 4$, $C_2 = -3.7 \times k/itr + 4$ and $w = 2 - 1.8 \times k/itr$ [23], where *itr* is the maximum number of iterations. These coefficients are designed to optimize the solution-finding process by introducing greater randomness in the early stages of iteration and decreasing the range in the later stages. This approach enhances the performance of the algorithm. The fabrication of disc solar absorber structures can be achieved through established nanofabrication techniques, such as magnetron sputtering, electron beam lithography, and focused ion beam

lithography [24–26]. The fabrication process involves depositing alternating layers of metal (such as tungsten) and SiO$_2$ film using magnetron sputtering, followed by the gradual etching of a disk on each film from the top layer using a focused ion beam.

2.2. Performance of Solar Energy Absorber

Regardless of heat loss other than heat radiation, the photothermal conversion efficiency [27] for the solar absorber is

$$\eta_1 = \alpha - \frac{\varepsilon_a \sigma T^4}{CG_S} \tag{3}$$

In Equation (3), σ is the Stefan-Boltzmann constant, T is the operating temperature of the absorber, $G_S = 1000 \, \text{W/m}^2$ is the incident flux of the solar radiation, and this value is calculated from the solar radiation spectrum under AM1.5 standard. C is the solar concentration ratio which is the ratio of received solar flow density by the solar energy concentration in the system to the solar flow density G_S. For the solar energy thermoelectric system, the solar energy generation efficiency can be calculated by the following formula:

$$\eta_2 = \eta_{fld}\eta_1\eta_q \tag{4}$$

where η_{fld} denotes the efficiency of the solar concentration system, which is defined as the ratio of the incident solar power to the power concentrated onto the absorber. $\alpha, \varepsilon_a, \eta_q$ refers to the standard solar radiation absorption efficiency for AM1.5 standard and the heat radiation efficiency and heat-electricity conversion efficiency of the heat-electricity device, respectively. $\alpha, \varepsilon_a, \eta_q$ is represented by the following formula:

$$\alpha = \frac{\int_0^\infty \alpha(\lambda)G(\lambda)d\lambda}{\int_0^\infty G(\lambda)d\lambda} \tag{5}$$

$$\varepsilon_a = \frac{\int_0^\infty \varepsilon_a(\lambda)u(\lambda, T)d\lambda}{\int_0^\infty u(\lambda, T)d\lambda} \tag{6}$$

$$\eta_q = \frac{P_{out}}{P_{in}} \tag{7}$$

where $u(\lambda, T)$ is the blackbody radiation, $G(\lambda)$ is the spectral light intensity of the wavelength under AM1.5 standard, and $\alpha(\lambda)$ and $\varepsilon_a(\lambda)$ are spectrally selective solar absorber emissivity and absorptivity as a function of wavelength, which is equal at thermal equilibrium. The input and output energy of the heat energy utilization system can be represented by P_{in} and P_{out} in Figure 1, respectively.

3. Results

The devices were optimized using the method described in Section 2.1, with α as the objective function. The results of the optimization are presented in Table 1, and the material parameters were sourced from Palik [28]. The algorithm parameters are set as indicated in Table 2. This method offers a significant reduction in computational cost compared to traditional tuning methods because the number of devices to be calculated with traditional methods grows exponentially with the number of parameters. For example, with the manual tuning of a device with four parameters and one hundred points selected for each parameter, the number of devices to be calculated would be N $= 100^4$, which is several orders of magnitude greater than the number of devices calculated using our algorithm (N $= 3000$). The calculation time using an i7 8700u home-class computer varies depending on the metal material used in the lumerical FDTD calculation, with tungsten taking approximately 2250 min to calculate using the method described in Section 2.1. This demonstrates the significant advantage of our method for absorber design.

Table 1. Solar Device Parameter Table (Length unit: nm). The total thickness is $H = h_0 + h_1 + h_2 + h_3 + h_4$. where $h_0 = 150$ nm. This thickness is sufficient to effectively reduce the transmittance of sunlight to nearly zero.

Metal Materials	The Number of Disk Layers	α	l_0	l_1	l_2	l_3	l_4	h_1	h_2	h_3	h_4	H
W	2	90.9%	404.8	114.2	199.2			113.1	40.7			304
W	4	95.5%	490.0	102.7	159.8	204.9	218.3	128.0	49.1	46.1	76.0	450
Ti	2	93.6%	416.9	119.4	181.6			129.0	40.2			319
Ti	4	97.6%	416.9	96.9	139.6	184.3	188.9	129.0	40.2	81.0	54.5	454
Cr	4	96.9%	466.7	94.7	181.1	198.3	221.8	127.3	45.3	40.0	92.4	455
V	4	88.9%	450.1	40.6	94.1	109.0	204.9	143.6	59.0	74.1	82.0	508

Table 2. Algorithm parameter setting.

Value Range of l_0	Value Range of $(l_1 \sim l_4)$	Value Range of $(h_1 \sim h_4)$	m	itr	Each Layer of N	Calculation Time
(300 nm, 600 nm)	(40 nm, 600 nm)	(40 nm, 200 nm)	20	150	3000	2250 min

It can be observed that the performance limits attainable by different material devices and stacks are not uniform. The discs represented by (l_1, h_1) and (l_3, h_3) are composed of SiO_2, while the discs represented by (l_2, h_2) and (l_4, h_4) are made of the metallic materials listed in Table 1. The maximum thickness of the devices is less than 508 nm, and the use of precious metals is avoided, thereby reducing cost and expanding the application range of the devices.

The absorption A, reflection R, and transmission T (1 = A + R + T) of the four-layer circular disk solar absorber in Table 1 for W are shown in Figure 4a. The absorption rate in the spectral range of 0.35 μm–1.7 μm is above 90%, with over 95% of the solar energy concentrated in this band. There is a perfect broadband absorption in the 0.7 μm–1.2 μm band. Our results demonstrate the absorption of AM1.5 solar spectrum by the device, as shown in Figure 4b, where most of the solar radiation can be captured with only less than 5% being reflected. In Equation (5), the absorption rate α is 95.6% within the wavelength range of 0.3 μm–14 μm.
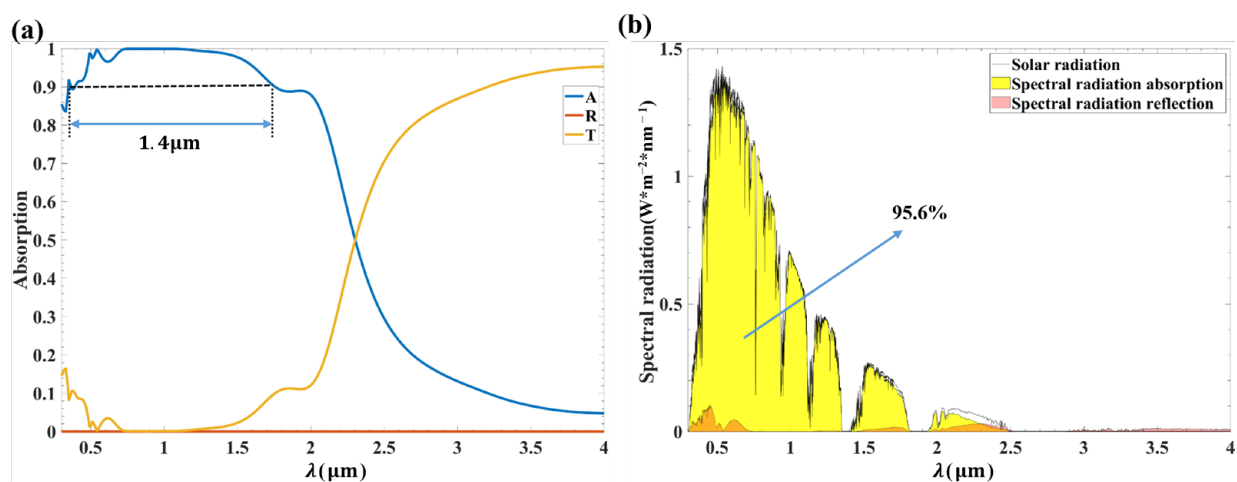

Figure 4. (a) Absorption (A), reflection (R), and transmission (T) spectra of the four-layered disk solar absorber of W. (b) Absorbed energy and lost energy of four-layer disk solar absorber of W.

Assume the absorber spectrum is ideal, as shown in Figure 5a, where the cut-off wavelength λ_c is the wavelength separating perfect absorption from perfect non-absorption. It is being examined how the maximum efficiency of photothermal conversion, denoted as η_1, and its corresponding absorption spectrum vary at different operating temperatures T and solar concentration ratio C. η_1 is positively correlated with α and negatively correlated with ε_a in Equation (1). Increasing T shifts the blackbody radiation spectrum to the left in Figure 5a, which increases the emissivity ε_a to a large extent, thus resulting in a decrease in device performance; ε_a has a stronger effect on performance at higher T values. The addition of λ_c in the Figure 5a increases the solar energy absorption (red area) and energy emission (yellow area). When λ_c is lower, the range of absorbed wavelength is narrower, leading to a lower α and less energy emission. In this case, the increase of T has little effect on the device's work efficiency. Conversely, when λ_c is larger, the range of absorbed wavelength is wider, resulting in a higher α and more energy emission. The increase of T will lead to a rapid decrease in work efficiency due to increased radiation loss. As shown in Figure 5b, the maximum work efficiency decreases with rising T. Increasing C can reduce the proportion of radiation loss and improve work efficiency. However, C exponentially increases, and the absorption rate increases linearly, so C is not likely to be too high. As shown in Figure 5c,d, the work efficiency decreases sharply when T increases to a certain extent. Improving C can greatly expand the high-efficiency work range. At the same time, because most of the energy of AM1.5 standard is below 1.2 μm, η_1 exceeds 0. 8 when $\lambda_c < 1.2$ μm. These conclusions can guide the design of absorber devices at specific T and C. For high operating temperatures, λ_c should be reduced appropriately and vice versa.
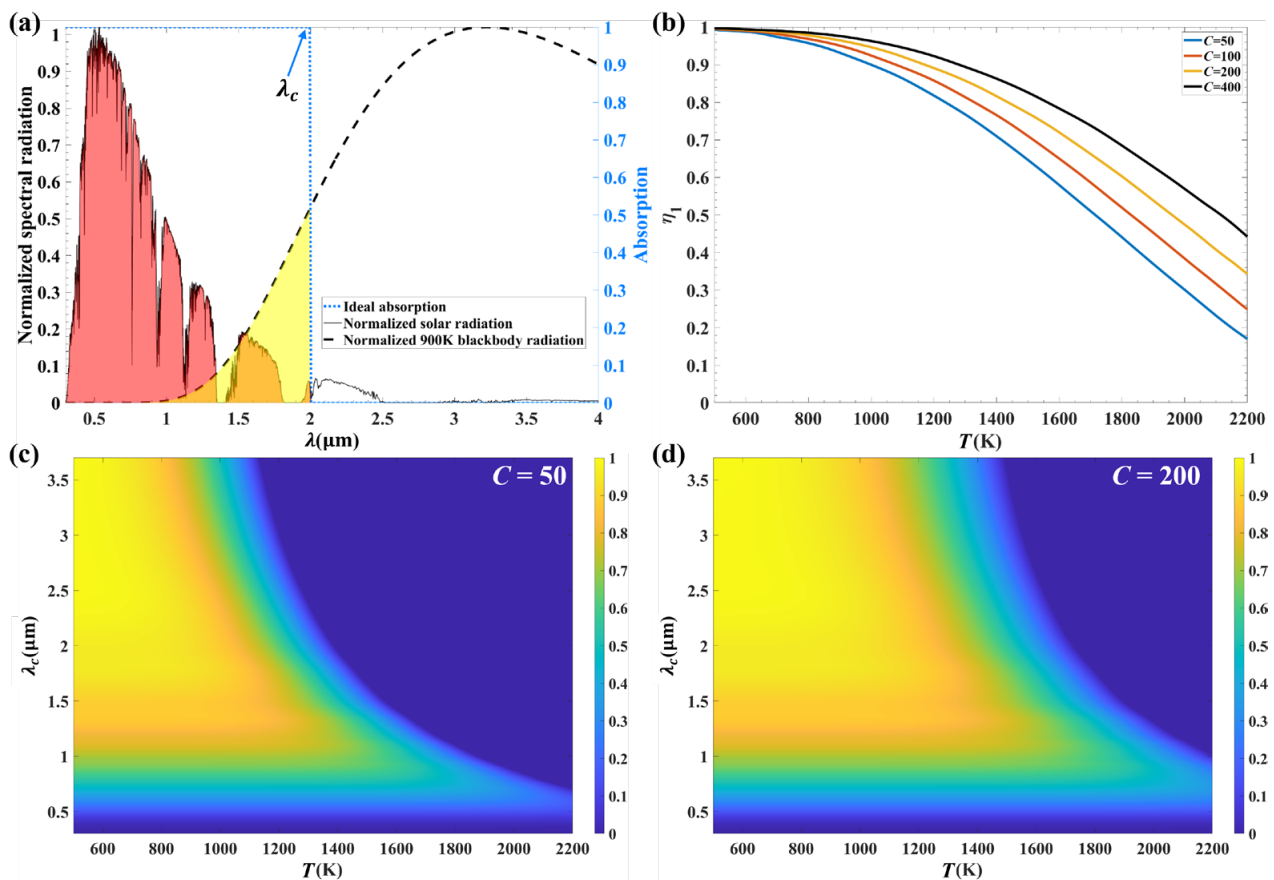

Figure 5. (**a**) The absorption of the solar spectrum is the red part, and the yellow part is the emitted heat radiation with the ideal absorption spectrum. (**b**) The maximum photothermal conversion efficiency η_1 variation with operating temperature at different condensing coefficients. (**c**,**d**) η_1 versus operating temperature T and cut-off wavelength λ_c with $C = 50$ and $C = 200$, respectively.

The absorption curves of a four-layer solar absorber comprised of Ti, Cr, W, and V, as outlined in Table 1, are presented in Figure 6a. Figure 6c,d reveal that the distinct dielectric constants of these metals lead to diverse optimization of the absorption performance. A qualitative analysis was conducted to investigate the effect of metal materials on the maximum absorption rate. The rate of change of the dielectric constant with respect to wavelength is W ≈ V > Cr > Ti, and the approximate cut-off wavelength relationship is W ≈ V < Cr < Ti. As described in the previous analysis, due to the gradual change in dielectric constants and high emissivity of Ti and Cr in the 0.3 μm–4 μm range, it leads to considerable heat loss under high operating temperature conditions. Therefore, Ti and Cr are the preferred metal materials for devices with low operating temperatures. Figure 6c exhibits that the trend and magnitude of the dielectric constant variation for W and V are highly consistent, resulting in their emissivity rates being also highly consistent and low, making them more appropriate for high-temperature applications. The visible band absorption rates of all four metal materials are lower than those in the infrared band. All four materials exhibit an absorption peak near the solar radiation peak of AM1.5 radiation, but there is a sharp decrease in the absorption of Cr, V, and W in the 0.4 μm–0.5 μm range, while Ti illustrates an absorption peak. Ti remains the most effective absorber (with an average absorption rate of 98.5%) within the visible band. Overall, the suitability order of metal materials for different operating temperature ranges is W ≈ V > Cr > Ti. Therefore, using W as the preferred metal material for the absorber under high-temperature conditions has benefits, as it has higher absorption than V, lower cost in comparison to V, and a significantly higher melting point than V.
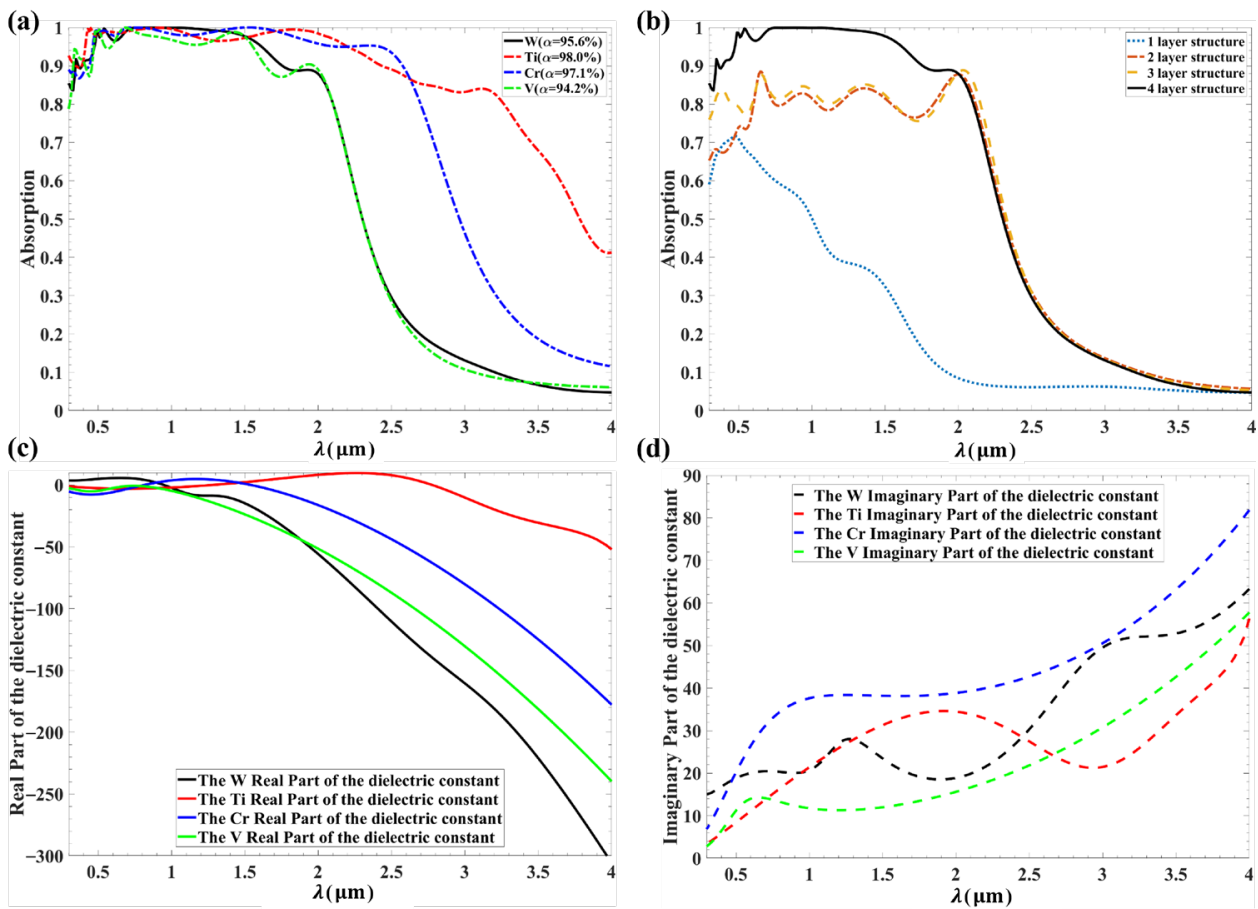

Figure 6. (**a**) Absorption curves of a four-layered disk solar absorber composed of Ti, Cr, W, and V. (**b**) Absorption curves of four-layer disk devices of W at different layer numbers. (**c**,**d**) represent the real and imaginary parts of the dielectric constants of the metals of W, Ti, Cr, and V.

The material choice and the number of disk stacking layers both significantly impact the absorption performance of the device. As depicted in Figure 6b, the absorption rate increases across all frequency ranges as the number of disk stacking layers increases. When there are two or three stacked layers, the absorption rate is relatively similar, with only a slight increase in the 0.3 µm to 0.5 µm band. This is due to the lack of increased absorption in the third layer of SiO$_2$ stacked. Figure 7 illustrates that the energy is primarily concentrated in the cavity surrounding the metal disks and between them, which is a result of the enhanced electric field caused by local surface plasmons between the metal surfaces. A Fabry-Perot (FP) cavity can be formed not only between alternating stacked metallic materials but also in the lateral direction. This allows for the coupling of FP cavity resonance and surface plasmon elements, resulting in enhanced optical fields for the device. The electric field distribution around a 509 nm wavelength is primarily concentrated around the top metal disk, leading to a relatively high peak value of the electric field intensity. Conversely, the electric field around 991 nm is mainly distributed in the lateral space between the second layer metal disks of the array, resulting in a more dispersed energy distribution and a lower peak value of the electric field intensity. This suggests the more cavities and boundaries between metals that can excite plasma resonances, the stronger the absorption capacity.
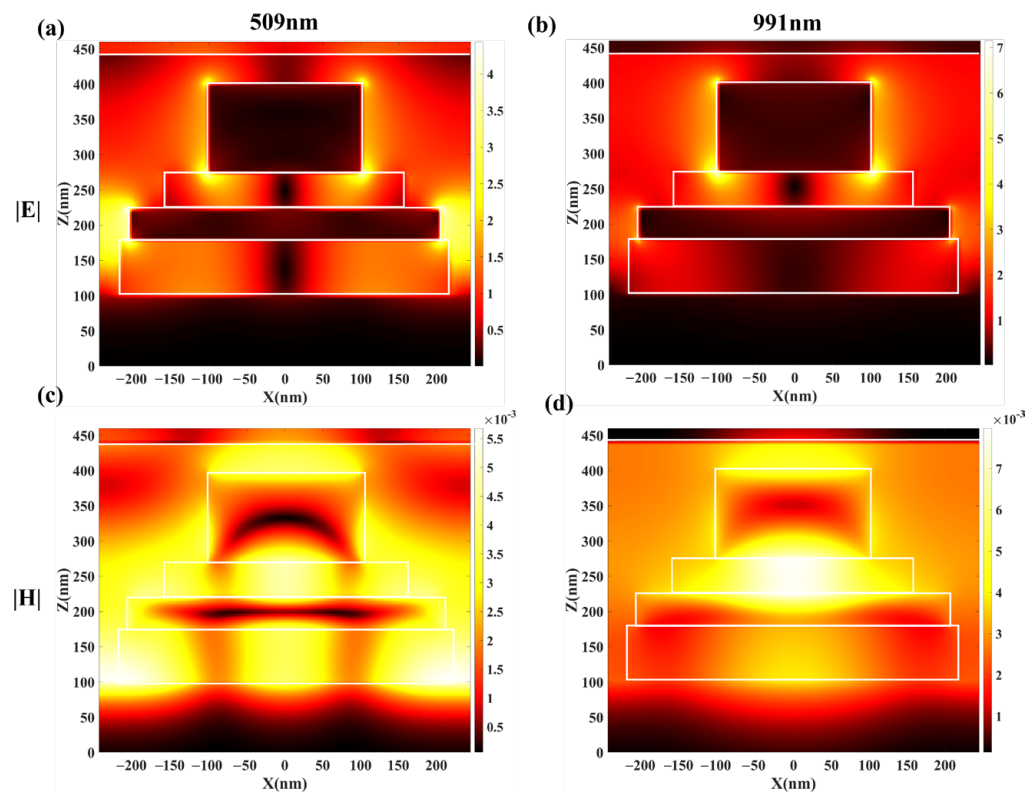

Figure 7. (**a**,**c**) Magnetic field intensity and electric field in the indicated XZ cross-sections at 509 nm wavelengths. (**b**,**d**) Magnetic field intensity and electric field in the indicated XZ cross-sections at 991 nm wavelengths.

In Figure 8, the impact of temperature on four different devices in $C = 200$ is depicted. The specific device structures can be found in Table 1. The photothermal conversion efficiency η_1 is significantly influenced by the emissivity, with the emissivity of Ti solar absorption devices being higher than that of W solar absorption devices. The four-layer Ti device has the fastest decrease in η_1 with an increase in operating temperature, and its α value is lower than that of the four-layer W device. As the emissivity gap between two-layer and four-layer W devices increases with the increase in operating temperature, two-layer W devices are the optimal choice when $T > 1110$ K. In general, at $C = 200$, for

operating temperatures lower than $T < 790$ K, a four-layer device made of Ti material is recommended. For $T \in (790 \text{ K}, 1110 \text{ K})$, a four-layer device made of W material is advised. Additionally, for $T < 1110$ K, a two-layer device made of W material is recommended. The performance of a two-layer structure may not be as optimal as that of a four-layer structure at $T < 1110$ K, but the manufacturing cost of the two-layer structure is more economical. As shown in Figure 8b, η_1 of the four-layer device is higher than that of the two-layer device at temperatures below 1110 K, but the difference is less than 4.6%. Nevertheless, the efficiency of the two-layer device is still over 90% at $T < 1110$ K. So, cost and performance should be weighed in practical applications.
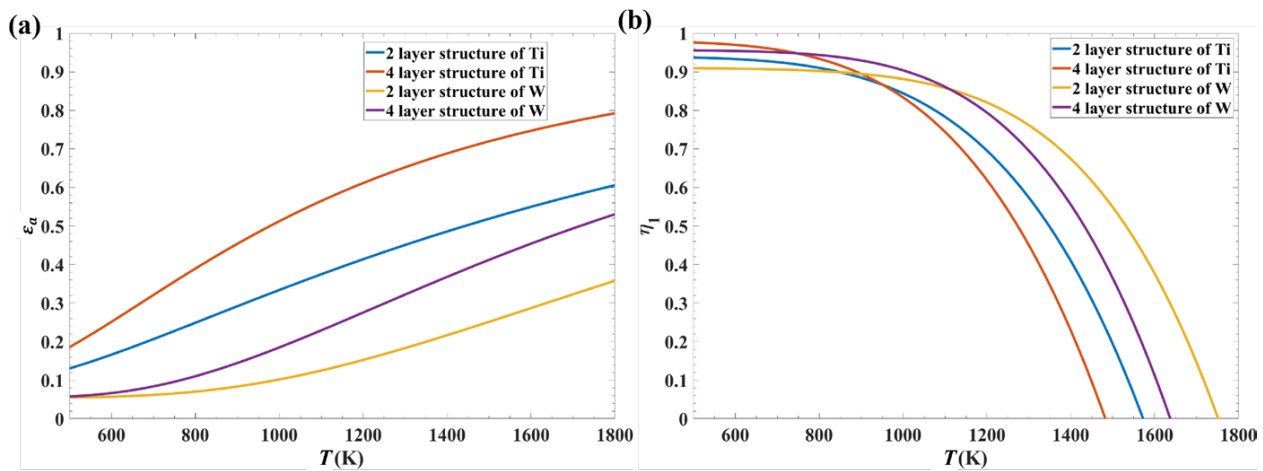
Figure 8. (**a**,**b**) are the emissivity ε_a and photothermal conversion efficiency η_1 of the four devices as a function of operating temperature T when $C = 200$, respectively.

In practical applications, it is crucial to examine the impact of the incident angle and polarization angle of the light source on the performance of a four-layer W disk solar absorber. As seen in Figure 9a, the change in polarization angle from $0°$ to $60°$ had no effect on the absorption spectrum of the solar absorber. The stacked disk structure has perfect symmetry making the device insensitive to incident light with different polarization angles. The absorption spectra of the device at incident angles of $0°$ to $60°$ are shown in Figure 9b. The change in incidence angle resulted in some decreases in α in the visible band, negatively impacting α and η_1, as seen in Figure 9c. Despite large angle deflections of the incident light, the device still maintains a high absorption efficiency. When the incidence angle is less than $39°$, the device's α and η_1 stayed above 90% and 86%, respectively.

The solar absorber, such as a thermoelectric generator, a TPV generator, or a thermionic convertor, converts the absorbed solar energy into thermal energy and then utilizes a thermoelectric conversion system to produce electrical energy. Since thermal engine efficiency is typically determined by the temperature difference, most thermoelectric systems require high working temperatures. Hence, reliable thermal management is necessary to ensure that all components are operating in an efficient range. In a solar power generation system based on a coupled air turbine, steam turbine, and thermal tower, the heat absorbed by the thermal tower from the sun can be converted into electricity with an efficiency (η_q) of 50% at 973 K [29]. As shown in Figure 10, when $C > 85$, the thermoelectric conversion efficiency of solar power plants (η_2) can exceed 33% when $\eta_{fld} = 0.78$ [29]. Furthermore, disregarding cost factors, using a two-layered W solar device is more efficient when $C < 85$. Here is a chance for the working efficiency of solar thermoelectric systems to break through the S-Q limit with current thermoelectric technology.
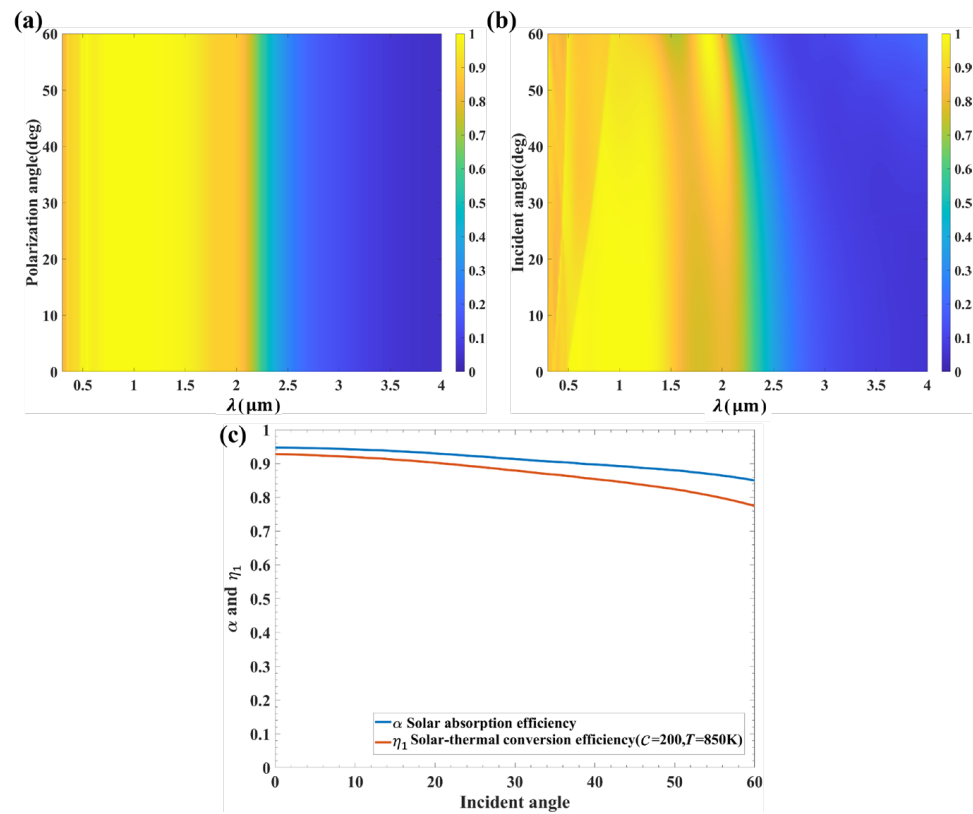
Figure 9. Absorption spectra of the four-layer disk device for W at different angles of incidence (**a**,**b**). (**c**) the emissivity ε_a and photothermal conversion efficiency η_1 of the four-layer disk device for W varies with the angle of incidence.
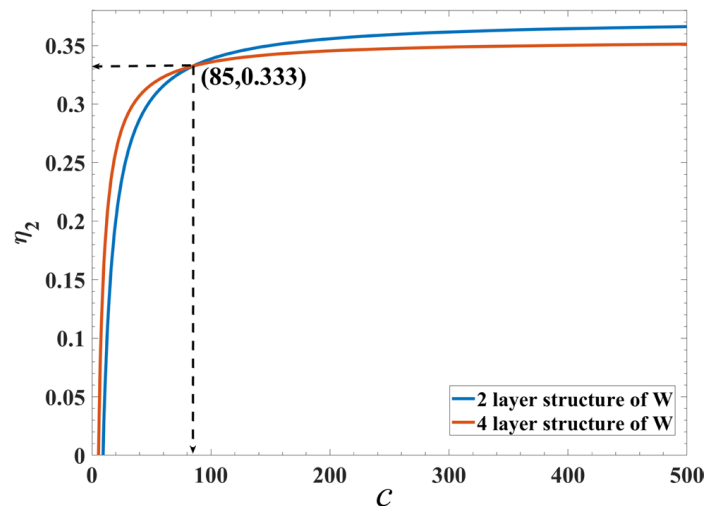

Figure 10. The relationship between the thermoelectric conversion efficiency and C for high-efficiency solar thermoelectric systems utilizing two-layered W and four-layered W solar absorbers.

4. Conclusions and Perspectives

In this work, we have employed modern optimization algorithms to efficiently design multiple multilayered circular stacked metasurfaces capable of highly efficient opto-thermal conversion under various conditions. One such device achieves an ultra-low emissivity of 5.7% ($T = 600$ K) in the range of 0.3 µm–14 µm while absorbing 95.5% of the solar spectrum. This approach is not only suitable for AM1.5 solar spectrum absorber design but also for AM0 solar spectrum absorber design in outer space and other spectral absorbers. Addition-

ally, the designed device, with its ultra-low emissivity and highly efficient absorption of the solar spectrum, has potential applications in infrared stealth, optoelectronic detection, and thermal imaging.

References

1. Farber, E.A. Selective Surfaces and Solar Absorbers. *Sol. Energy* **1959**, *3*, 9–13. [CrossRef]
2. Kumar, K.K.P.; Mallick, S.; Sakthivel, S. Cobalt-Rich Spinel Oxide-Based Wide Angular Spectral Selective Absorber Coatings for Solar Thermal Conversion Applications. *Renew. Energy* **2023**, *203*, 334–344. [CrossRef]
3. Cheng, P.; Wang, D.; Schaaf, P. A Review on Photothermal Conversion of Solar Energy with Nanomaterials and Nanostructures: From Fundamentals to Applications. *Adv. Sustain. Syst.* **2022**, *6*, 2200115. [CrossRef]
4. Behar, O.; Khellaf, A.; Mohammedi, K. A.; Mohammedi, K. A Review of Mature Solar Thermal Power Stations. In *Multivolume Book of Energy and Science*; LCC Stadium Press: New York, NY, USA, 2015.
5. Zhou, Z.; Chen, Q.; Bermel, P. Prospects for High-Performance Thermophotovoltaic Conversion Efficiencies Exceeding the Shockley–Queisser Limit. *Energy Convers. Manag.* **2015**, *97*, 63–69. [CrossRef]
6. Manor, A.; Kruger, N.; Sabapathy, T.; Rotschild, C. Thermally Enhanced Photoluminescence for Heat Harvesting in Photovoltaics. *Nat. Commun.* **2016**, *7*, 13167. [CrossRef]
7. Zhao, B.; Hu, M.; Ao, X.; Xuan, Q.; Song, Z.; Pei, G. Is It Possible for a Photovoltaic-Thermoelectric Device to Generate Electricity at Night? *Solar Energy Mater. Solar Cells* **2021**, *228*, 111136. [CrossRef]
8. Liu, M.; Steven Tay, N.H.; Bell, S.; Belusko, M.; Jacob, R.; Will, G.; Saman, W.; Bruno, F. Review on Concentrating Solar Power Plants and New Developments in High Temperature Thermal Energy Storage Technologies. *Renew. Sustain. Energy Rev.* **2016**, *53*, 1411–1432. [CrossRef]
9. Aydin, K.; Ferry, V.E.; Briggs, R.M.; Atwater, H.A. Broadband Polarization-Independent Resonant Light Absorption Using Ultrathin Plasmonic Super Absorbers. *Nat. Commun.* **2011**, *2*, 517. [CrossRef]
10. Li, Y.; Liu, Z.; Zhang, H.; Tang, P.; Wu, B.; Liu, G. Ultra-Broadband Perfect Absorber Utilizing Refractory Materials in Metal-Insulator Composite Multilayer Stacks. *Opt. Express* **2019**, *27*, 11809. [CrossRef]
11. Shen, F.; Kang, Q.; Wang, J.; Guo, K.; Zhou, Q.; Guo, Z. Dielectric Metasurface-Based High-Efficiency Mid-Infrared Optical Filter. *Nanomaterials* **2018**, *8*, 938. [CrossRef]
12. Jiang, X.; Yuan, H.; Chen, D.; Zhang, Z.; Du, T.; Ma, H.; Yang, J. Metasurface Based on Inverse Design for Maximizing Solar Spectral Absorption. *Adv. Opt. Mater.* **2021**, *9*, 2100575. [CrossRef]
13. Tian, Y.; Han, L.; Yan, L.; Wang, J.; Zhang, B.; Jiao, Z. Optically-Controlled Terahertz Multifunctional Polarization Conversion Metasurface with Reflection and Transmission Modes. *Micromachines* **2022**, *13*, 1387. [CrossRef]
14. Piggott, A.Y.; Lu, J.; Lagoudakis, K.G.; Petykiewicz, J.; Babinec, T.M.; Vučković, J. Inverse Design and Demonstration of a Compact and Broadband On-Chip Wavelength Demultiplexer. *Nature Photon.* **2015**, *9*, 374–377. [CrossRef]
15. Jiang, X.; Wang, T.; Zhong, Q.; Yan, R.; Huang, X. A Near-Ideal Solar Selective Absorber with Strong Broadband Optical Absorption from UV to NIR. *Nanotechnology* **2020**, *31*, 315202. [CrossRef] [PubMed]
16. Liu, J. Inverse Design a Patternless Solar Energy Absorber for Maximizing Absorption. *Solar Energy Mater. Solar Cells* **2022**, *244*, 111822. [CrossRef]
17. Zhang, W.-W.; Qi, H.; Yu, Z.-Q.; He, M.-J.; Ren, Y.-T.; Li, Y. Optimization Configuration of Selective Solar Absorber Using Multi-Island Genetic Algorithm. *Sol. Energy* **2021**, *224*, 947–955. [CrossRef]

18. Burlafinger, K.; Vetter, A.; Brabec, C.J. Maximizing Concentrated Solar Power (CSP) Plant Overall Efficiencies by Using Spectral Selective Absorbers at Optimal Operation Temperatures. *Solar Energy* **2015**, *120*, 428–438. [CrossRef]
19. Cao, F.; McEnaney, K.; Chen, G.; Ren, Z. A Review of Cermet-Based Spectrally Selective Solar Absorbers. *Energy Environ. Sci.* **2014**, *7*, 1615. [CrossRef]
20. De Maio, D.; D'Alessandro, C.; Caldarelli, A.; Musto, M.; Russo, R. Solar Selective Coatings for Evacuated Flat Plate Collectors: Optimisation and Efficiency Robustness Analysis. *Solar Energy Mater. Solar Cells* **2022**, *242*, 111749. [CrossRef]
21. Chowdhary, A.K.; Reddy, V.A.; Sikdar, D. Selective Thermal Emitters for High-Performance All-Day Radiative Cooling. *J. Phys. D Appl. Phys.* **2022**, *55*, 085504. [CrossRef]
22. Sheehan, D.P. Infrared Cloaking, Stealth, and the Second Law of Thermodynamics. *Entropy* **2012**, *14*, 1915–1938. [CrossRef]
23. Ratnaweera, A.; Halgamuge, S.K.; Watson, H.C. Self-Organizing Hierarchical Particle Swarm Optimizer With Time-Varying Acceleration Coefficients. *IEEE Trans. Evol. Computat.* **2004**, *8*, 240–255. [CrossRef]
24. Ariga, K.; Hill, J.P.; Ji, Q. Layer-by-Layer Assembly as a Versatile Bottom-up Nanofabrication Technique for Exploratory Research and Realistic Application. *Phys. Chem. Chem. Phys.* **2007**, *9*, 2319. [CrossRef]
25. Kelly, P.J.; Arnell, R.D. Magnetron Sputtering: A Review of Recent Developments and Applications. *Vacuum* **2000**, *56*, 159–172. [CrossRef]
26. Chason, E.; Picraux, S.T.; Poate, J.M.; Borland, J.O.; Current, M.I.; Diaz de la Rubia, T.; Eaglesham, D.J.; Holland, O.W.; Law, M.E.; Magee, C.W.; et al. Ion Beams in Silicon Processing and Characterization. *J. Appl. Phys.* **1997**, *81*, 6513–6561. [CrossRef]
27. Bermel, P.; Ghebrebrhan, M.; Chan, W.; Yeng, Y.X.; Araghchini, M.; Hamam, R.; Marton, C.H.; Jensen, K.F.; Soljačić, M.; Joannopoulos, J.D.; et al. Design and Global Optimization of High-Efficiency Thermophotovoltaic Systems. *Opt. Express* **2010**, *18*, A314. [CrossRef] [PubMed]
28. Palik, E. *Handbook of Optical Constants of Solids*; Elsevier: Amsterdam, The Netherlands, 1985; ISBN 978-0-08-054721-3.
29. Li, J.-F.; Lyu, J.-F.; Xu, N. Analysis of High Efficient Solar Thermal Power Generation System. *J. Eng. Thermophys.* **2020**, *41*, 1308–1317.